PAPER

Check for updates

Hydrothermal synthesis and characterization of the antimony–tin oxide nanomaterial and its application as a high-performance asymmetric supercapacitor, photocatalyst, and antibacterial agent

Eswaran Amutha,[a] Subramanian Rajaduraipandian,[b] Minnalkodi Sivakavinesan [ID][a] and Gurusamy Annadurai [ID] *[a]

We have synthesized antimony-tin oxide (ATO) nanoparticles chemically for use in antibacterial, photocatalytic, and supercapacitor applications. The XRD pattern reveals the hexagonal structure, while the FTIR spectra validate the functional groups. The agglomerated nanostructures, which are 40–50 nm thick and 100 nm long, are shown in the SEM images as having spherical, cube, square, and rod form morphologies. In a DLS test, ATO has a zeta potential of 28.93/−28.00 mV, demonstrating strong colloidal stability in the suspension. With minimum inhibitory concentrations (MIC) ranging from 25 to 100 g mL^{-1}, ATO is also tested for its antibacterial activity against a variety of Gram-positive and Gram-negative bacteria. Additionally, rhodamine dye was broken down by ATO nanoparticles in 240 minutes with a degradation efficiency of 88 percent. The specific capacitance (C_s) and energy density (E) values of ATO nanoparticles further demonstrated their suitability for use in supercapacitors.

1. Introduction

Researchers have created revolutionary clean renewable energy storage technologies in response to energy issues and environmental damage.[1] Due to their exceptional qualities, such as high power density, long lifetime, and a quick charge/discharge process, supercapacitors, a type of energy conversion and storage devices, have drawn a lot of attention.[2,3] There have been numerous reports of nanostructured materials for use in supercapacitors.[4] It was thought that these nanostructured materials outperform bulk materials in terms of capacitance.[5]

Since they have fast charging times, high power densities, and long cycle lives over repeated charge and discharge times, supercapacitors-one of the most popular electrical energy storage devices—are attractive candidates for backup power, cell phone cameras, regenerative braking, and hybrid electric vehicles.[6,7]

Tin oxide is one of the significant wide direct band gap semiconductors ($E_g = 3.6$ eV) at RT with a lot of excellent applications in various fields, for example, chemical sensors, lithium-ion batteries, solar cells, catalysis, *etc.*[8] Tin oxide (SnO_2)

possesses a wide energy gap and be regarded as an n-type semiconductor oxide.[9] Antimony (Sb) as an n-type dopant is one of the most common dopants for SnO_2. The dopant Sb modifies the SnO_2 structure, such as the band structure.[10] The lattice structure of SnO_2 greatly increases after the addition of Sb atom into tin oxide solution. The electron conductivity of the nanomaterial increases with the increase in crystal lattice planes.[11,12] A Sb atom can be regarded as an excellent conductive doped material. A SnO_2 doped Sb atom (ATO) possesses high conductivity that provides a high tunnel for the easy transfer of electrons between the electrode material and electrolyte.[13]

Nanoparticles have long been known for their antimicrobial behavior against Gram-positive and Gram-negative bacteria, pathogens, and other microbes.[14] Metal oxide nanoparticles serve as antimicrobial agents owing to their large surface area. Out of several metal oxide nanomaterials, scientists have more interest in SnO_2 nanoparticles because of their novel properties such as high chemical stability, high transparency, low electrical sheet resistance, *etc.*[15] Other than these applications, SnO_2 has received attention as an antimicrobial agent and has played an essential role against the growth of various bacterial strains like *Staphylococcus aureus*, *Bacillus subtilis*, *Enterobacter* sp., *Pseudomonas fluorescens*, and *Escherichia coli*.[16]

Dyes from textile, paper, and other industries are prime examples of environmental contaminants. Among these methods, photocatalytic degradation of dyes using UV light is one of the most prominent techniques because the reactions

[a]Sri Paramakalyani Centre of Excellence in Environmental Sciences, Manonmaniam Sundaranar University, Alwarkurichi - 627412, India. E-mail: gannadurai@msuniv.ac.in

[b]Sri Paramakalyani College, Manonmaniam Sundaranar University, Alwarkurichi - 627412, India

are carried out under ambient conditions that are cost-effective and simple.[17] Various photocatalysts like TiO_2, ZnO, WO_3, CeO_2, and ZrO_2 nanoparticles are used for degradation of organic dyes. Out of these catalysts, ATO nanoparticles have been proven to be competent photocatalysts for environmental applications because of their strong redox ability, nontoxicity, long-term stability, and low cost. However, metal oxides such as TiO_2, SnO_2, ZnO have been found to be better photocatalysts for the degradation of organic dyes in aqueous solution.[18] SnO_2 as an *n*-type semiconductor has also been reported for the degradation of various azo dyes. Besides antimicrobial activities, ATO finds improved results in photocatalytic activities.[13]

The creation of antimony tin oxide (ATO) nanoparticles utilising the hydrothermal method under UV light irradiation was discussed in terms of catalysis, high performance asymmetric supercapacitor and antibacterial research. Ultraviolet-visible (UV-vis) spectroscopy, Fourier transform infrared (FT-IR) spectroscopy, X-ray diffraction (XRD) analysis, dynamic light scattering (DLS) analysis, and scanning electron microscopy (SEM) were used to evaluate the produced ATO nanoparticles.

2. Materials and methods

2.1 Chemicals, reagents, and media

Sigma Aldrich Pvt Ltd, in India, supplied analytical grade tin chloride, antimony chloride, ethanol, polyvinyl pyrrolidone (PVP), poly vinyl alcohol (PVA), and ethylene glycol. Gram-positive *Staphylococcus aureus* and *Bacillus subtilis*, as well as Gram-negative *Escherichia coli*, *Enterobacter* sp., and *Pseudomonas fluorescens* bacterial isolates, were purchased from MTCC, Chandigarh.

2.2 Synthesis of antimony tin oxide (ATO) nanoparticles

Antimony tin oxide (ATO) nanoparticles were synthesized using the hydrothermal method. Using a magnetic stirrer, 100 mL of ethanol and distilled water were combined with 0.06 M of tin chloride and 0.04 M of antimony chloride. The solution was heated steadily and vigorously for 30 minutes to combine the two salts into a homogenous mixture. Then, 1 g of PVP and PVA were gradually added, drop by drop, to the aforementioned mixture. To the aforementioned solution 10 mL of ethylene glycol solution was added and constantly swirled for 30 minutes. The mixture was sealed in a Teflon autoclave with a capacity of 100 mL and kept at 120 °C for 12 hours and cooled to ambient temperature. The precipitate was centrifuged and then washed numerous times with distilled water and ethanol. The particles are then dried for 24 hours in a hot air oven at 80 °C. The particles are then annealed for 2 hours at 600 °C (Scheme 1).

2.3 Electrochemical measurement

Electrochemical behavior of ATO nanoparticles was examined using cyclic voltammetry (CV), galvanostatic charge–discharge (CD), and electrochemical impedance spectroscopy (EIS). The working electrode was created by mixing nanocomposite materials in a 85 : 15 : 10 weight ratio with conductive carbon
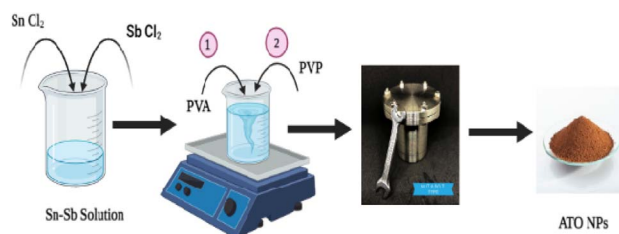
Scheme 1 Synthesis of ATO nanoparticles.

(carbon black) and binder (PDFE). The resulting electrode paste (~2 mg) was placed on a Ni foam current collector that had been pre-treated and employed as a working electrode. Electrochemical experiments were performed in a 3 M KOH electrolyte using a three-electrode cell with Pt foil as the counter electrode and Ag/AgCl as the reference electrode. Different scan rates and current rates were used in CV and CD investigations. The specific capacitance, energy density and power density of the system were calculated from the discharge profile by using the following formula:

$$C_{sp} = \frac{\int I \, dV}{mv\Delta V} \tag{1}$$

$$C_{sp} = \frac{I\Delta t}{m\Delta V} \tag{2}$$

2.4 Antibacterial properties

2.4.1 Agar well diffusion assay. Using the well diffusion method, the antibacterial ability of the ATO nanoparticles was tested using pathogenic bacteria such as Gram-positive *Staphylococcus aureus* and *Bacillus subtilis*, as well as Gram-negative *Escherichia coli*, *Enterobacter* sp., and *Pseudomonas fluorescens*. For the evaluation of antibiotic activity of the above bacterial species, different concentrations of 25 μL, 50 μL, 75 μL and 100 μL were utilised. All of the plates were incubated for 24 hours at 37 °C, and the zone of bacterial inhibition was determined.

2.5 Photocatalytic activity and kinetic studies

The photocatalytic performance of ATO nanoparticles was assessed by measuring the photocatalytic degradation of rhodamine dye under UV irradiation. In a typical process, 0.1 g of ATO was added to 100 mL of aqueous rhodamine dye solution with a 1 ppm starting concentration. The suspension of ATO nanoparticles and dye solution was agitated in the dark for 30 minutes prior to irradiation to reach adsorption/desorption equilibrium. The suspension was then exposed to UV radiation. Approximately 2 mL of the suspension was withdrawn from the combination at regular intervals (30 minutes) and centrifuged to separate the photocatalyst particles during irradiation. The concentration of rhodamine solution in the supernatant was then measured using a UV-vis spectrophotometer, which has a distinctive absorbance at $\lambda_{max} = 550$ nm.

The degradation efficiency was calculated using the formula mentioned below:

$$\text{Degradation efficiency} = \frac{c_0 - c}{c_0} \times 100\% \qquad (3)$$

where C_o = initial rhodamine dye concentration, and C = concentration of the rhodamine dye solution after degradation time 't'.

The kinetics of the photodegradation of rhodamine dye was investigated using the Langmuir–Hinshelwood model.[19] The following pseudo-first-order equation, according to this approach, can describe the reaction's kinetics:

$$\ln(C_0/C) = kt + s \qquad (4)$$

where s is a constant parameter that represents the photo-catalyst's adsorption capacity, k is the rate constant (min^{-1}), and t is the irradiation time (min).

2.6 Embryo toxicity test

The embryonic developmental stage of a zebrafish embryo was studied under a stereomicroscope for the whole exposure period following fertilisation. For 24–96 hpf, the embryos were treated to doses of ATO nanoparticles (0, 25, 50, 100, and 200 μg mL^{-1}). Every 24 hours, the hatching rate and embryonic death were assessed. The ratio of hatching embryos to the remaining viable embryos in each well is known as the hatching rate. The embryos and larvae from the control and treatment groups both had malformations that were documented and photographed. A stereomicroscope (Optica, Italy Model; T3 15 A) was used to image the deformed embryos, and every 24 hours, the proportion of malformed embryos was recorded.

2.7 Characterization of ATO nanoparticles

The chemical composition of the synthesized ATO nanoparticles was studied by using an FTIR spectrometer (PerkinElmer LS-55-Luminescence spectrometer). The phase variety and grain size of the synthesized ATO nanoparticles were determined by X-ray diffraction spectroscopy (Philips PAN analytical). Dynamic light scattering (DLS) which is based on the laser diffraction method with multiple scattering techniques was employed to study the average particle size of ATO nanoparticles (ZETA sizer Nanoseries, Malvern instrument Nano Zs). TGA is considered as the most important method for studying thermal stability of polymers and nanoparticles. The thermal stability of the ATO nanoparticles was investigated by using a TGDTA (Hitachi-Thermo Gravimetry/Differential Thermal Analyzer STA7000, Japan). The scanning electron microscopic analysis was done using a Carl Zeiss Evo 18 secondary electron microscope with an EDS machine with the magnification up to 50–100 K depending on the sample. Fluorescence characterization of the ATO Nanoparticles was performed using an Instrument model L S4 5.

3. Results and discussion

3.1 Fourier transform infrared spectroscopy

The FT-IR spectra of the produced ATO nanoparticles was analysed to determine the groups responsible for nanoparticle capping and stability. Fig. 1 shows the FTIR spectra of the as-
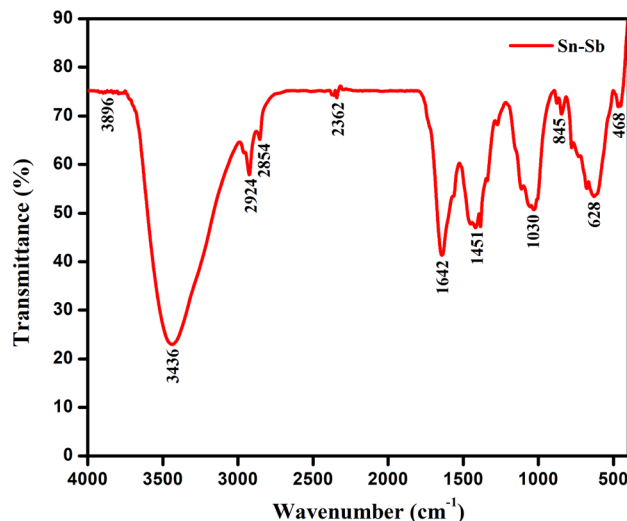

Fig. 1 FTIR spectrum of ATO nanoparticles.

prepared materials, determined in the frequency[20] range of 4000 to 350 cm^{-1}.

The presence of a peak at 3896 cm^{-1} was for the O–H stretch of alcohols and a peak at 3436 cm^{-1} corresponds to the O–H stretch of H–bonded alcohols and phenols. The peak located at 2924 and 2854 cm^{-1} corresponds to the stretching mode vibration of the C–H stretch of alkanes. The absorption peak at 1642 cm^{-1} might be due to the C=C stretch (conjugated) of alkenes.[21] The peaks at 1451 cm^{-1} and 1030 cm^{-1} represent the C–F stretching of alkyl halides and C–C stretch of ketones. The peaks at 845 cm^{-1} correspond to C–H bend of (mono) aromatics. The peaks at around 628 cm^{-1} are for acetylenic C–H bend alkynes, and the one at 468 cm^{-1} for C–X stretch of bromoalkanes.

3.2 Structural analysis

The crystallinity and phase purity of the ATO nanoparticles was characterized by using X-ray diffraction (XRD) in the diffraction
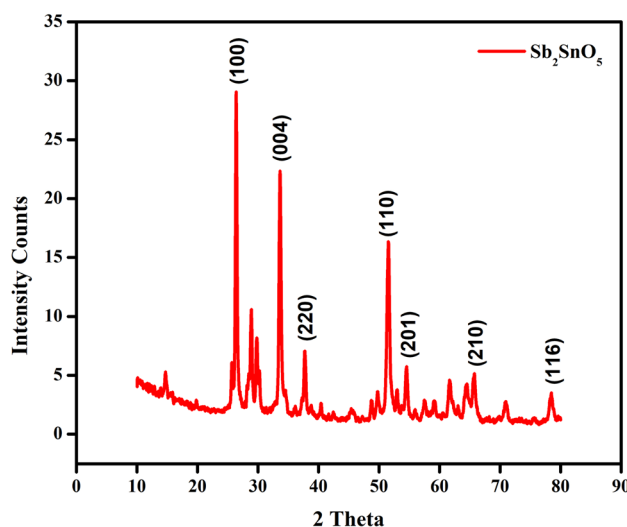

Fig. 2 XRD pattern of ATO nanoparticles.

angle (2θ) ranges between 10° to 80° with a scanning rate of 5° per minute. The XRD pattern of ATO nanoparticles contains several peaks as shown in Fig. 2. The obtained XRD characteristics peaks show that the intensity peaks were observed at 17.61°, 25.64°, 28.08°, 29.61°, 33.98°, 42.94° and 50.2° corresponding to the (hkl) values of the peaks (100), (004), (220), (110), (201), (210) and (116). The well extended intensity peaks indicate the polycrystalline nature and size reduction of ATO.[22] All the identified ATO nanoparticle peaks are in good agreement with the JCPDS card number 73-2141 and LCSD card number 4242. It clearly indicates the formation of hexagonal structured ATO.

The average crystallite size of the ATO nanoparticles was found by using the Debye–Scherrer formula, where K is a constant (0.91), λ is the wavelength of the X-ray ($\lambda = 1.5418$ Å), θ is the diffraction angle for the peak and β is the full width at half maximum (FWHM).[5] The average crystallite size of the samples synthesized by this method is 32.24 nm.[23]

3.3 Particle size analyzer

Dynamic light scattering (DLS) was used to determine the size distribution of ATO nanoparticles. The DLS method measures the amount of scattered light travelling through a nanoparticle solution. The average size distribution of the ATO nanoparticles is 55 nm, as shown in Fig. 3.

3.4 Thermogravimetric analysis

The TGA of dried ATO nanoparticles aged in air for 24 hours at optimal concentration before being analysed in nitrogen at a heating rate of 20 °C min^{-1}, as shown in Fig. 4. In the temperature range of 50–80 °C, the first weight loss was 17.10 mg in ATO. The second weight loss occurred at 130–129 °C, which was attributed to water evaporation from Sb–SnCl$_2$ during the production of ATO nanoparticles.[24] The third weight loss was at 210–216 °C, which is due to Sb–SnCl$_2$ breakdown. In the temperature range of 430–422 °C, a sharp weight loss of 16.97 mg in ATO was observed. Then Sb–SnCl$_2$ decomposes to generate SnO and CO$_2$, resulting in a 28 percent weight loss.[8]

3.5 Scanning electron microscopy (SEM) and EDAX

Fig. 5 shows SEM imaging of the ATO nanoparticles. The structure and morphological behaviour of the bimetallic
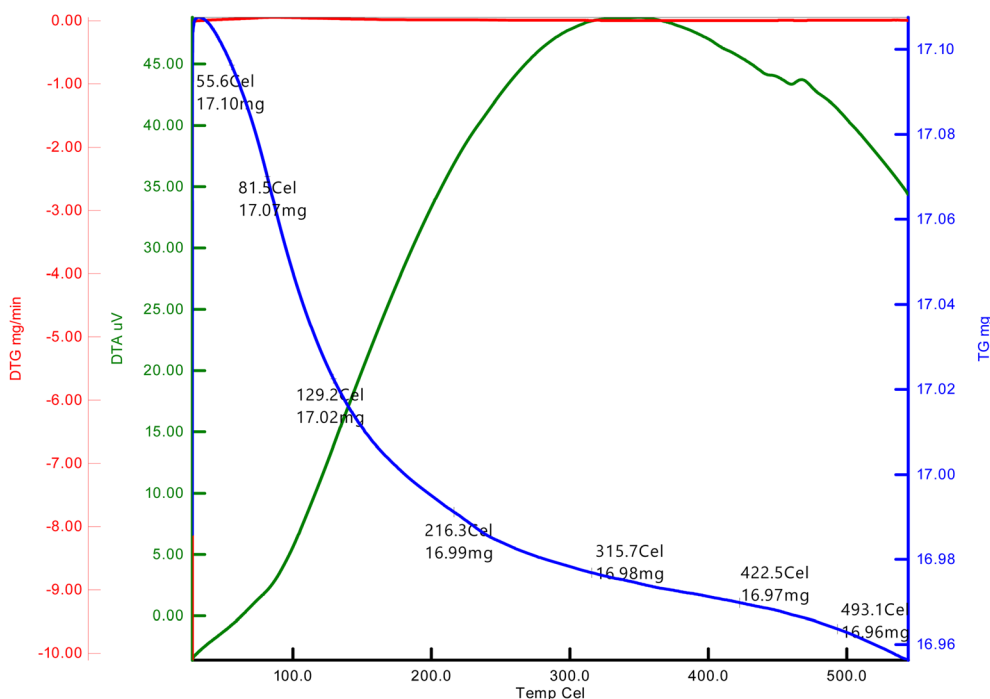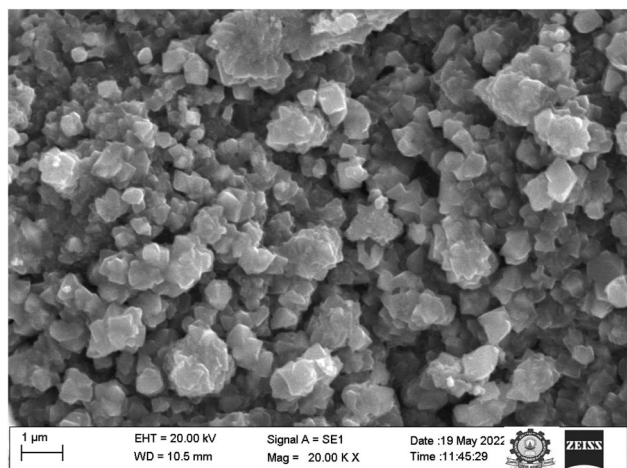

Fig. 3 PSA image of ATO nanoparticles.

Fig. 4 TGA image of ATO nanoparticles.

© 2023 The Author(s). Published by the Royal Society of Chemistry

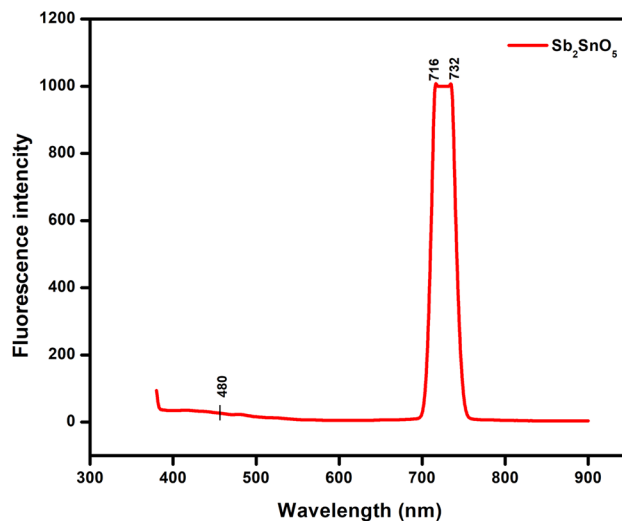**Fig. 5** SEM image of ATO nanoparticles.

Fig. 7 Fluorescence spectrum of ATO nanoparticles.

nanoparticles are supported by SEM images. When PVP and PVA were utilised as reducing and capping agents, distinct morphologies of ATO nanoparticles were produced.[25] With agglomerated nanostructured ATO nanoparticles, ATO nanoparticles produced approximately spherical, cube, square, and rod shapes, respectively. This could be owing to the fact that different chemical compounds have varied quantities and types of capping agents. The shifts and differences in the regions of the peaks found in the FTIR study also support this.[26]

EDX analysis was carried out to understand the semi quantitative elemental composition of ATO nanoparticles. The peaks showed the presence of antimony and tin (Fig. 6) particles. The total metal content was quite high to justify the purity of metallic nanoparticles.[27]

3.6 Fluorescence spectroscopy

A fluorescence spectrophotometer was used to characterize the fluorescence spectra of the ATO nanoparticles, as shown in

Fig. 7. The fluorescence spectrum is an excellent tool for determining energy levels.[28]

Fig. 7 shows the fluorescence spectra of ATO nanoparticles measured with an excitation wavelength. At 716 and 732 nm, the fluorescence (FL) band's centre appears. The fluorescence intensity increased as the size of the ATO nanoparticles grew larger. The intensity of the fluorescence emission band and the absorption band of ATO nanoparticles were both concentration and particle size dependent, according to these findings.[29]

3.7 The energy storage mechanism

The supercapacitor, as depicted in Scheme 2, is primarily made up of numerous elements, including current collectors, electrodes, electrolytes, and separators. The role of separator is similar to the separator in the battery. In addition to allowing ions to pass through, it isolates the two electrodes to prevent short circuits between the electrodes. Supercapacitors work on the simple premise that they can store electrical energy by
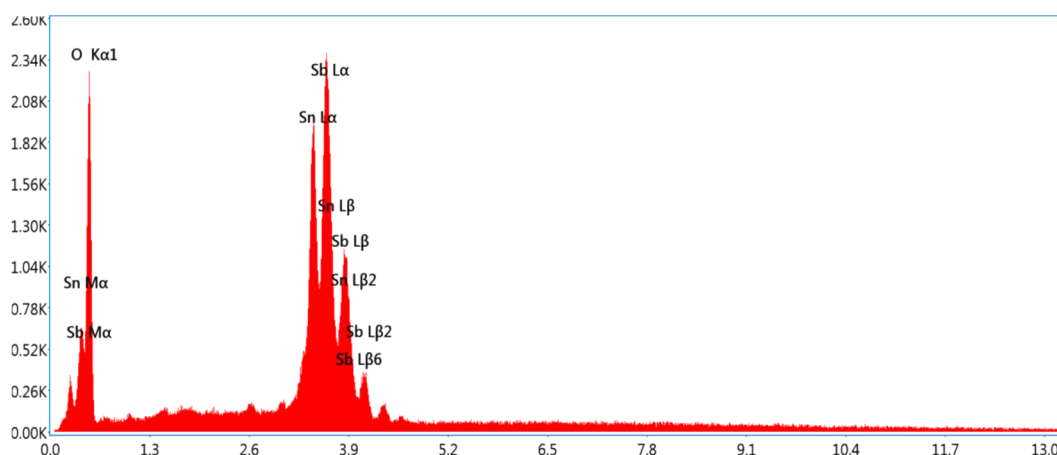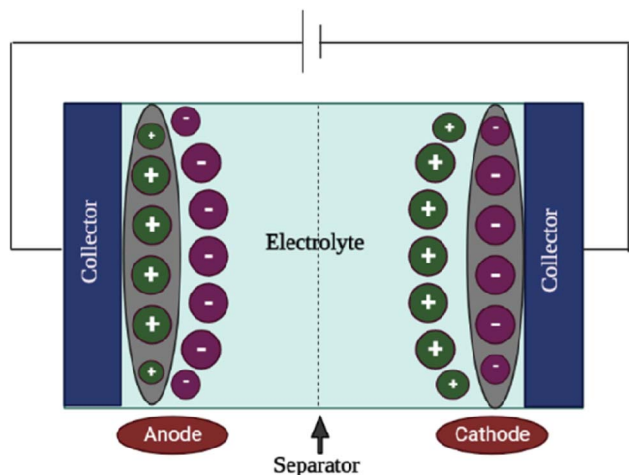

Fig. 6 EDAX spectrum of ATO nanoparticles.

Scheme 2 Mechanism of a supercapacitor.

forming an electric double-layer capacitance at the interface between the electrolyte and the bath solution.

3.8 Electrochemical studies

Using cyclic voltammetry (CV) in a 3 M KOH solution, the electrochemical behaviour of the produced nano-crystalline electrode materials (ATO) for electrochemical capacitors
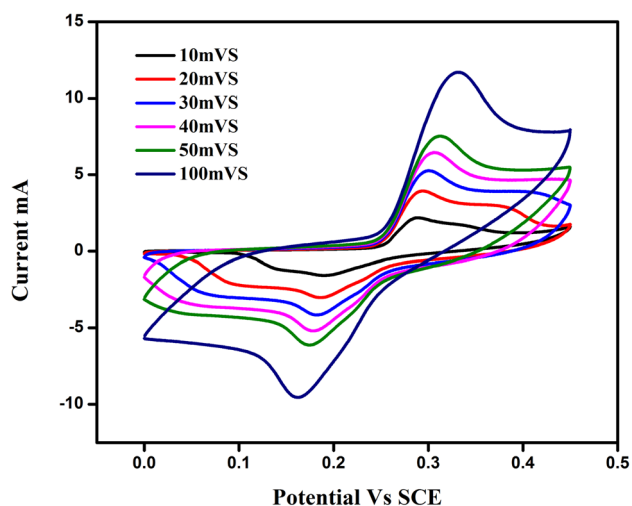

Fig. 8 Cyclic voltammogram obtained on ATO nanostructured electrode materials at different scan rates in 3 M KOH electrolyte.

was investigated. The CV experiments were carried out at different scan rates (5, 10, 20, 30, 40, 50, and 100 mV s^{-1}), with the findings displayed in Fig. 8. The CV tests were carried out with a potential voltage range of 0.7 to 0.4 V vs. SCE. The cyclic voltammograms of all samples were rectangular and oval in form, indicating that a typical pseudocapacitve response occurs at the graphite electrode/active material (ATO)/electrolyte interface, as stated.[30] By resembling a pseudocapacitive nature, these CV curves improve as scan rates increase. Furthermore, as the scan rate is increased, the current increases because the electrolyte ions have more time to penetrate into the pores of the material at lower scan rates, whereas at higher scan rates, they are only collected on the electrode's outermost surface due to current dependence on the scan rate.[31] The CV curves varied from one another, which could be owing to the various concentrations of ATO nanoparticles. The specific capacitance values were calculated as per eqn (2):

$$C_{sp} = \frac{\int I \, dV}{mv\Delta V} \tag{1}$$

$$C_{sp} = \frac{I\Delta t}{m\Delta V} \tag{2}$$

where $\int I \, dV$ is the absolute surface area, 'S' is the scan rate, 'M' is the mass of active material and 'ΔV' is $V_2 - V_1$ = potential window. The specific capacitance values calculated for ATO nanoparticle nanostructured materials at different scan rates are shown in Table 1. Among the electrode materials, ATO nanoparticles resulted in a superior specific capacitance (56.49 F g^{-1}) at a scan rate of 10 mV s^{-1}.

Galvanostatic charge discharge (GCD) tests were carried out in a 3 M KOH solution to better understand the electrochemical characteristics of electrode materials such as ATO nanoparticles. The results are displayed in Fig. 9. The charge–discharge curves of ATO nanoparticle based electrode materials were obtained at current densities ranging from 0.5 to 20 A g^{-1}. All of the GCD curves had a symmetrical triangle, indicating that optimal capacitor behaviour was present in all of the samples.[32]

EIS measurements were used to look into the charge transport kinetics of the electrode materials. As reported, the Nyquist plot offers data on equivalent series resistance (ESR), electrode–electrolyte interactions, and interfacial effects. The EIS study of ATO nanoparticle electrode materials was performed with an amplitude of V in the frequency range of 1 Hz to 1 kHz. Fig. 10 show the Nyquist plots produced on ATO bimetallic nanoparticle electrode materials. The Nyquist plot depicted a straight line that was nearly parallel to the imaginary

Table 1 Specific capacitance data obtained for ATO nanoparticles

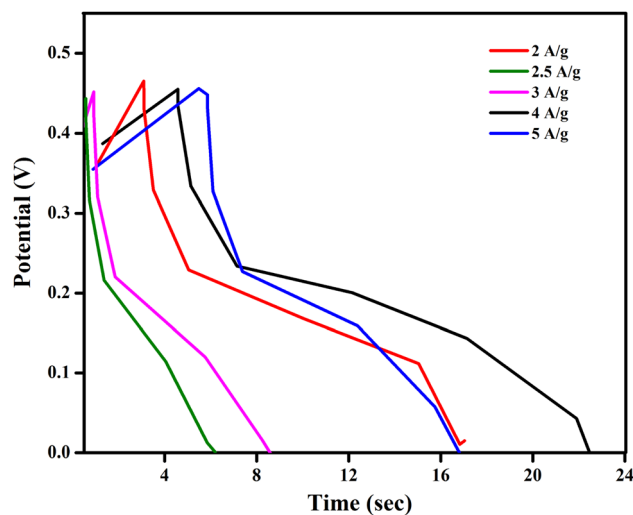| Specific capacitance values at different scan rates					
Electrode material	100 mV s^{-1}	50 mV s^{-1}	40 mV s^{-1}	30 mV s^{-1}	20 mV s^{-1}	10 mV s^{-1}
ATO	84.53 F g^{-1}	66.4 F g^{-1}	66.6 F g^{-1}	62.33 F g^{-1}	55.94 F g^{-1}	51.67 F g^{-1}

Fig. 9 Galvanostatic charge–discharge curves obtained on ATO nanostructured electrode materials at different current densities.
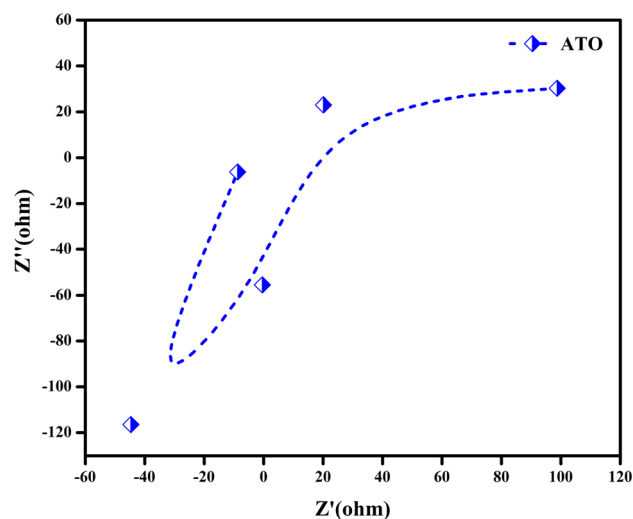

Fig. 10 Nyquist plots obtained for ATO nanostructured electrode materials.

components. The presence of perfect capacitance behaviour in all four samples is revealed by the straight line obtained in the low frequency range, as described.[27] Furthermore, the EIS spectrum generated from the intercept at the actual impedance axis is a mixture of electrode/electrolyte resistance, internal resistance of the active material, electrolyte interface resistance, and electrode/current collector contact resistance.[33] The Warburg behaviour resulting from rapid ion diffusion across the electrolyte/electrode interface is related to the straight line slope of the low frequency area in the Nyquist plot. As a result, we can conclude that supercapacitors can display optimal capacitive behaviour at low frequencies and blocking behaviour at high frequencies.[34] It is possible that this study may reveal a clear

method for making ATO nanoparticle-based electrode materials for high-performance supercapacitors.[35]

3.9 Antibacterial activity

The agar well diffusion method was used to test the antibacterial activity of integrated ATO nanoparticles against *Staphylococcus aureus*, *Bacillus subtilis*, *Enterobacter* sp., *Pseudomonas fluorescens*, and *Escherichia coli* (Fig. 11).

Pathogenic bacteria (24 hour culture) were cultured in a nutrient broth and swabbed uniformly onto separate plates with Mueller Hinton agar using a sterile L-rod. Purified ATO nanoparticles of various concentrations, such as 25 μL, 50 μL, 75 μL and 100 μL, were added to each well on all plates. The plates were incubated in an incubator, for 24 hours at 37 °C. The varying amounts of zone formation surrounding the well were measured after incubation.[36] The results in Table 2 indicate that the nanoparticles are more effective against *E. coli* than against other bacterial strains. The greater biocidal efficiency of ATO nanoparticles for *E. coli* is due to the difference in the cell wall structure between Gram negative and Gram positive microorganisms.

3.10 Photocatalytic properties of ATO nanoparticles

The photocatalytic activity of the ATO nanoparticles was investigated by choosing the photocatalytic degradation of rhodamine dye as a model system. The characteristic absorption peak at 520–540 nm of rhodamine dye was used for monitoring the catalytic degradation process. The absorption spectra of aqueous solution of rhodamine dye tested at different time intervals in the presence of ATO nanoparticles are shown in Fig. 12. The main absorption peak at 520 nm decreased gradually with the extension of the exposure time, indicating the photocatalytic degradation of rhodamine dye. Under UV irradiation, the produced ATO nanoparticles decolorized rhodamine dye by 88 percent in about 240 minutes, implying that ATO nanoparticles are capable of complete dye molecular breakdown. In the absence of nanocatalysts (control) the reaction did not have any progress. Literature in photocatalysis research reveals that photocatalytic activity can be strongly dependent on the crystallographic structure, morphology, and size of the particles.[18]

3.10.1 Mechanism of photocatalytic catalytic degradation of the dye. Scheme 3 depicts the degradation of rhodamine dye as a light-dependent process. The dye is first adsorbed on the surface of the catalyst (in this example, ATO), and then exposed to ultraviolet light to excite valence electrons and allow them to move from the valence band to the conduction band; a positive hole h^+ is lifted inside the valence band during this process. Positive holes and free electrons react with adsorbed water molecules on the photocatalyst's surface, yielding ˙OH radicals, while free electrons convert dissolved oxygen to superoxide anion $O_2\cdot$ radicals. These light generated radicals breakdown the dye molecules into simpler molecules like CO_2 and H_2O.
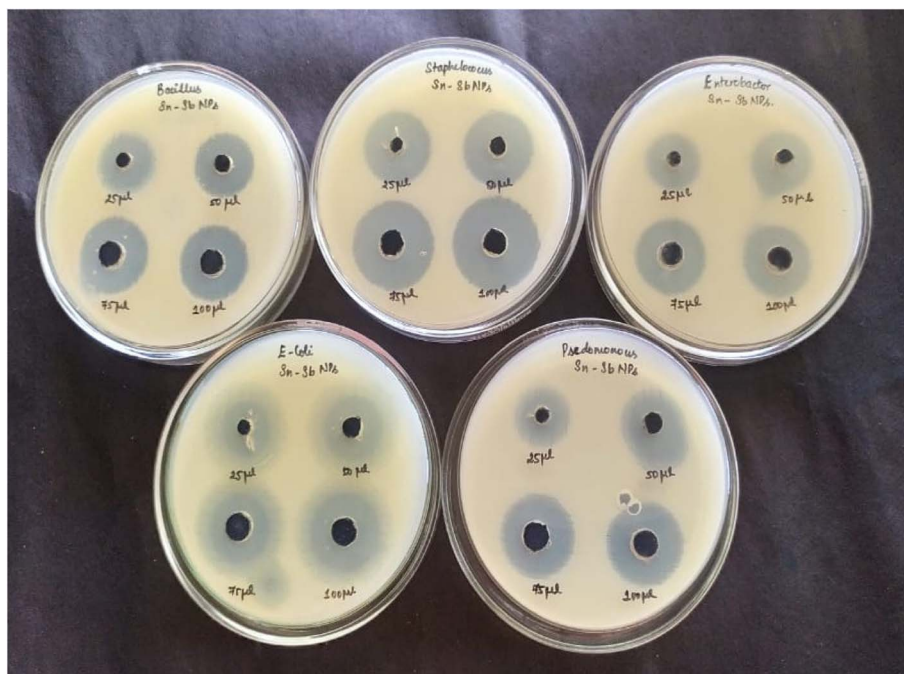
$$ATO + h\nu \rightarrow e^- + h^+ \qquad (5)$$
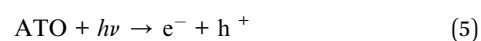
Fig. 11 Zone of inhibition of ATO nanoparticles against various bacterial strains.

Table 2 Zone of inhibition of ATO nanoparticles against selected bacterial strains

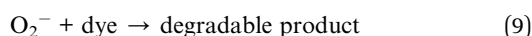|	Zone of inhibition (cm in diameter)				
Concentration	*Bacillus subtilis*	*Escherichia coli*	*Enterobacter* sp.	*Staphylococcus aureus*	*Pseudomonas fluorescens*
25 μL	1.6	1.8	1.8	2.0	0.8
50 μL	1.8	2.2	2.1	2.1	0.9
75 μL	2.1	2.5	2.2	2.4	1.1
100 μL	2.4	2.7	2.6	2.6	1.1
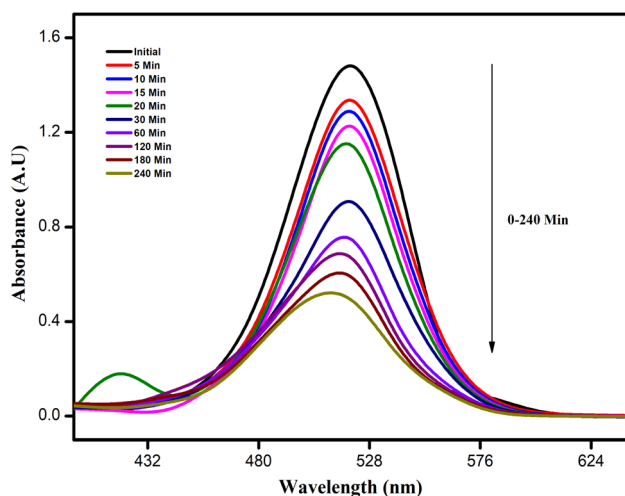
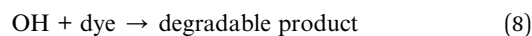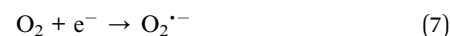**Fig. 12** UV-visible spectra of rhodamine dye with ATO nanoparticles. Rhodamine dye degradation using the as-prepared photocatalyst

$$H_2O + h^+ \rightarrow OH^\cdot + H^+ \tag{6}$$

$$O_2 + e^- \rightarrow O_2^{\cdot -} \tag{7}$$

$$OH + dye \rightarrow degradable\ product \tag{8}$$

$$O_2^- + dye \rightarrow degradable\ product \tag{9}$$

The photocatalytic degradation of rhodamine dye under UV light irradiation was used to assess the photocatalytic activity of the photocatalyst in its as-prepared state. The rhodamine dye solution naturally has a pH of 6.8, a starting rhodamine dye concentration of 0.6 mg L^{-1}, and a photocatalyst dose (ATO nanoparticles) of 0.1 g L^{-1}. The photocatalytic tests were carried out at various times (hours). Fig. 13 shows the charts of C/C_0 *versus* time. Rhodamine dye's concentration is seen to marginally drop in the dye solution with the photocatalyst, demonstrating its photostability when exposed to UV light. The photocatalyst exhibits rhodamine dye absorption upon UV light exposure. Rhodamine dye ATO nanoparticles had an adsorptive
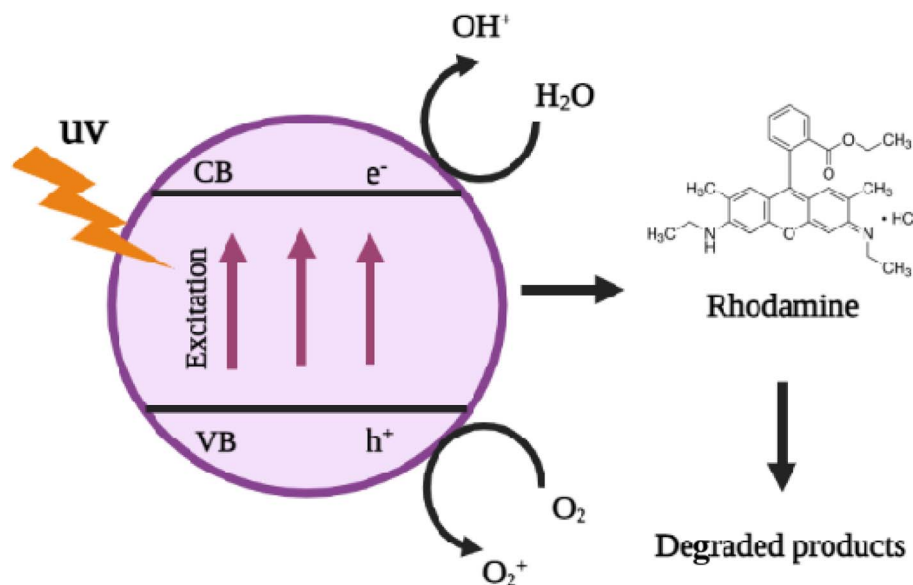
Scheme 3 Reaction mechanisms for the degradation of rhodamine.

removal efficacy of 88%, correspondingly. The greater adsorption capacity of the ATO nanoparticles favours photocatalytic degradation as a result. Rhodamine dye concentration reduced as a result of light irradiation, and after 70–170 minutes of exposure, rhodamine dye removal efficiency increased. More active sites are made available to the dye species and the breakdown rate of rhodamine dye is accelerated by higher adsorption capacity. This boosts the quantity of photogenerated electrons and holes and speeds up rhodamine dye's decomposition.[37]

3.10.2 Kinetics of rhodamine dye photodegradation. Fig. 14 displays the graphs of $\ln(C_0/C)$ with irradiation time. The derived correlation coefficients for the linear plots of Eqn (2) and data fitting both support the hypothesis that rhodamine dye is
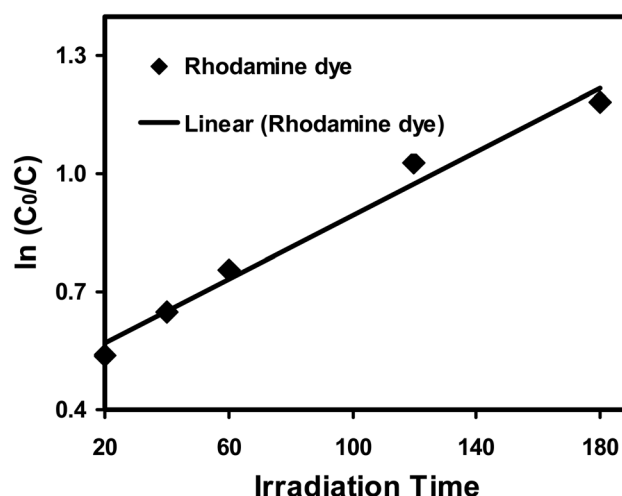

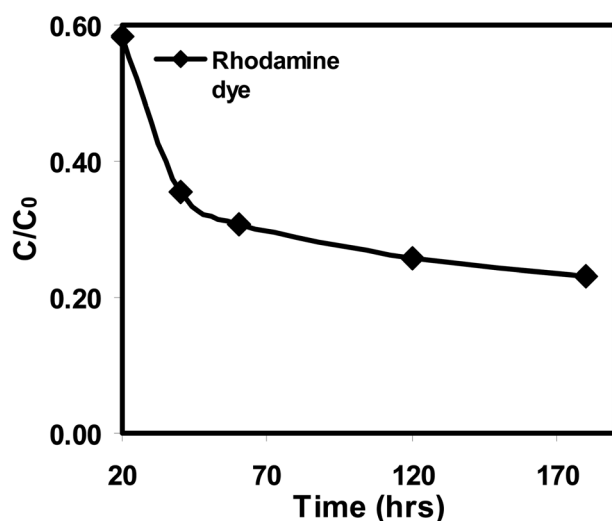**Fig. 14** Kinetic plots of the photodegradation of rhodamine dye for the photocatalyst.

photocatalytically degraded over ATO nanoparticles according to pseudo-first-order kinetics.[38,39] Under ideal circumstances, a pseudo-first-order rate constant of 0.004 min^{-1} was attained.

Adsorption and photodegradation are both effective ways to remove rhodamine dye, however at lower concentrations; adsorption predominates while photodegradation contributes less (Table 3). The ideal circumstances were attained with a catalyst dosage of 0.1 g L^{-1}, an initial rhodamine dye concentration of 0.6 mg L^{-1}, and an inherent pH of 6.8 for the rhodamine dye solution. A final removal efficiency of 88% was achieved under these circumstances (Fig. 16).

3.10.3 Toxicity study of the photocatalyst ATO nanomaterial. The ATO nanoparticles were shown to have excellent toxicity on the eggs of adult zebra fish, as seen in the Fig. 15. The concentration of 100 and 200 μL at 48 hours of exposure, at

Fig. 13 Plots of the photodegradation rate of rhodamine dye under UV light illumination for the photocatalyst.

Table 3 Comparative study of photocatalytic and biological activity of nanoparticles

Nanomaterial	Organism	Zone of inhibition	Reference
Zn/FeO	*Staphylococcus aureus*	No significant activity	40
	Escherichia coli		
Polyaniline/Ag–Pt	*Staphylococcus aureus*	30 ± 1.25 mm	41
AgAu	*Acinetobacter baumannii*	16 mm	42
	Staphylococcus aureus	8 mm	
	Escherichia coli	4 mm	
Ag–Cu	*Listeria monocytogenes*	No significant activity	43
	Salmonella enterica sv typhimurium		
Co@AgNP	*Escherichia coli*	8.51 mm	44
	Bacillus subtilis	4.41 mm	
AgPdNPs	*Staphylococcus aureus*	14 mm	45
	Pseudomonas aeruginosa	16 mm	
ATO	*Staphylococcus aureus*	26 mm	Our result
	Bacillus subtilis	24 mm	
	Enterobacter sp.	26 mm	
	Pseudomonas fluorescens	11 mm	
	Escherichia coli	27 mm	

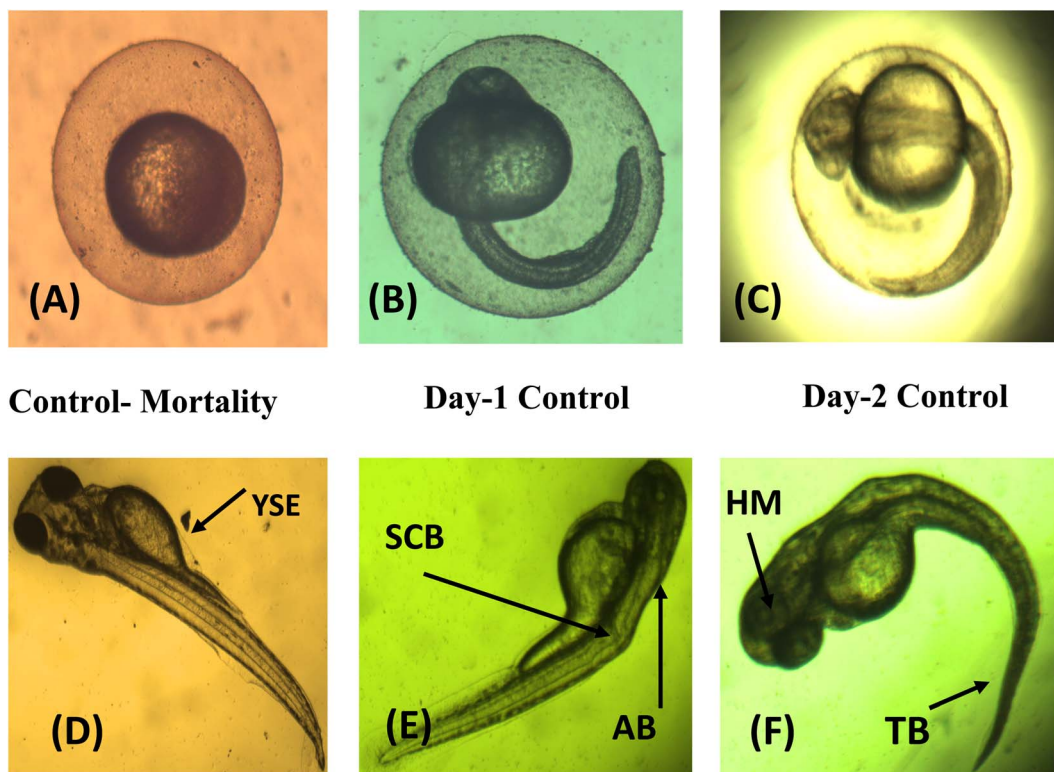| Type of catalyst	Light source	Type of pollutant	Concentration of pollutant	% of degradation	Reference
ZnS NPs	UV	RB5	20 ppm	100	46
CdS/Ni	UV	MO	15 ppm	98	47
Bi_2S_3/Fe_3O_4	Xe-lamp	CR	30 mg L^{-1}	91.60	48
Ag_2S/TiO_2	Visible	MO	20 mg L^{-1}	69	49
CdS NPs	Visible	MB	10 mg L^{-1}	83.8	50
ATO	UV	Rhodamine		86	Our result

Fig. 15 ATO nanoparticle imaging in zebrafish embryos and larvae. (A), (B) and (C) represents the control and mortality images of an ATO nanoparticle, (D) represents yolk sac edema (YSE) at 48 h, (E) represents spinal card bend (SCB) and axis bend (AB) at 72 h, (F) represents tail bend (TB) and head malformation (HM) at 96 h.
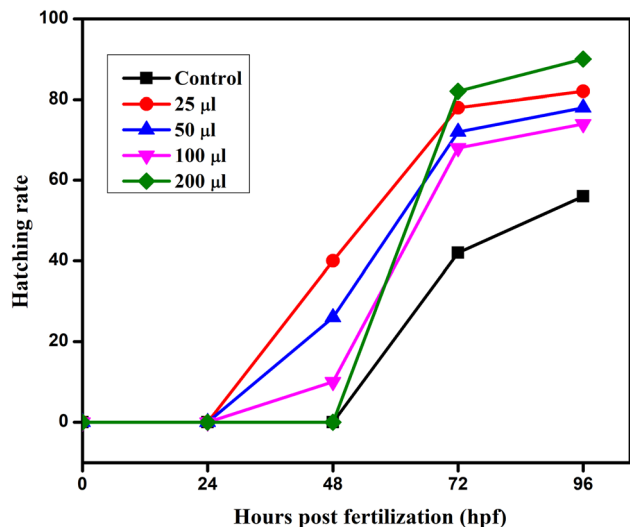
Fig. 16 Effects of ATO nanoparticles on hatching rates of zebrafish embryos from 24–96 hpf.
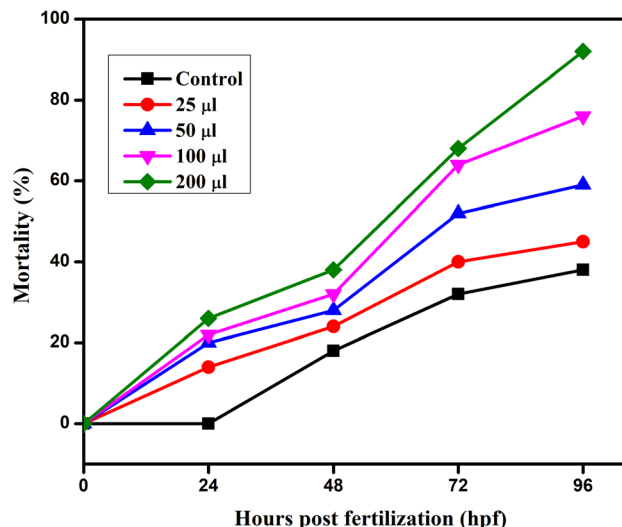

Fig. 18 Effects of ATO nanoparticles on mortality rates of zebrafish embryos from 24–96 hpf.
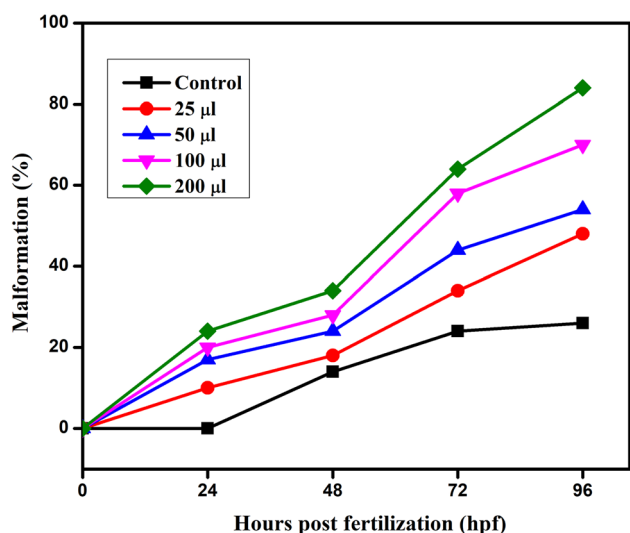

Fig. 17 Effects of ATO nanoparticles on malformation rates of zebrafish embryos from 24–96 hpf.

a value of LC 50, had good hatching rate capabilities on these adult zebrafish eggs. When the concentration of the ATO nanoparticles is increased, the malformation level likewise grows day by day. At a concentration level of 200 μL after 96 hours, the malformation of eggs reaches a high level (Fig. 17). Similar to this, the ATO nanoparticle mortality rate shows that at 200 μL of concentration, high mortality occurs at 96 hours, whereas eggs exposed to the control level likewise perished after 48 hours.[51] These differences make it abundantly evident that the toxicity of nanoparticles depended not only on the dose provided but also on the particle's size, shape, capping agent, stability, and aquatic medium's quality (Fig. 18).

4.   Conclusion

In this research study, a simple and direct hydrothermal method to prepare ATO nanoparticles was studied. X-Ray diffraction (XRD), scanning electron microscopy (SEM), Fourier transform infrared (FT-IR) spectroscopy, fluorescence spectroscopy (FL), a particle size analyser (PSA), and thermogravimetric analysis were used to evaluate the characteristics of ATO nanoparticles (TGA). The structural, optical, and thermal properties of ATO nanoparticles were confirmed based on the characterized results. A scanning electron microscopy study of the as-synthesized powders revealed spherical, cube, and rod shapes with agglomerated particles with diameters in the range of lower than 100 nm, according to XRD analyses. DLS is a method for determining the average particle size of bimetallic nanoparticles made of ATO. As a result, preparing ATO nanoparticles could be a useful tool in antibacterial research, allowing researchers to develop new antibodies for difficult-to-treat pathogens. At 240 minutes, the produced ATO nanoparticles were also effective in degrading rhodamine dye. The toxicity study of the photocatalyst was studied and the results showed that the photocatalyst has a negligible effect on zebra fish growth.

Conflicts of interest

The authors did not declare any conflict of interest.

Acknowledgements

References

1 M. Dashti Najafi, S. Kholghi Eshkalak, B. Amiri, H. R. Naderi, E. Kowsari, A. Chinnappan and S. Ramakrishna, *Mater. Today Chem.*, 2022, **23**, 100633.

2 Z. H. Mahmoud, R. A. AL-Bayati and A. A. Khadom, *J. Oleo Sci.*, 2022, ess21283.

3 Q. Xiong, B. Liu, Y. Liu, P. Wang, H. Cheng, H. Li, Z. Lu and M. Yang, *Nano Res.*, 2022, **15**, 7759–7768.

4 A. Subramanian, D. Karuppiah and B. Baskaran, *J. Electron. Mater.*, 2022, **51**, 3958–3969.

5 P. I. Ekwere, Microwave synthesized ruthenium antimony oxide-graphene nanocomposite materials for asymmetric supercapacitors, PhD thesis, 2022, http://etd.uwc.ac.za/xmlui/handle/11394/9097.

6 C. Mevada, P. S. Chandran and M. Mukhopadhyay, *J. Energy Storage*, 2020, **28**, 101197.

7 M. R. Zakaria, M. F. Omar, M. S. Zainol Abidin, H. Md Akil and M. M. A. B. Abdullah, *Composites, Part A*, 2022, **154**, 106756.

8 B. Saravanakumar, G. Ravi, V. Ganesh, F. Ameen, A. Al-Sabri and R. Yuvakkumar, *J. Sol-Gel Sci. Technol.*, 2018, **86**, 521–535.

9 S. Sivakumar, E. Manikandan, B. Mahalakshmi, N. Ahmad mala and L. Nelson prabu, *Vacuum*, 2020, **173**, 109116.

10 J. Zhang and L. Gao, *Mater. Res. Bull.*, 2004, **39**, 2249–2255.

11 H. Lee, S. Jin and S. Yim, *J. Phys. Chem. Solids*, 2020, **138**, 109264.

12 V. Velmurugan, U. Srinivasarao, R. Ramachandran, M. Saranya and A. N. Grace, *Mater. Res. Bull.*, 2016, **84**, 145–151.

13 M. M. Rahman, J. Ahmed and A. M. Asiri, *Sens. Actuators, B*, 2017, **242**, 167–175.

14 K. Chand, D. Cao, D. E. Fouad, A. H. Shah, M. N. Lakhan, A. Q. Dayo, H. J. Sagar, K. Zhu and A. M. A. Mohamed, *J. Mol. Liq.*, 2020, **316**, 113821.

15 D. Chandran, L. S. Nair, S. Balachandran, K. Rajendra Babu and M. Deepa, *J. Sol-Gel Sci. Technol.*, 2015, **76**, 582–591.

16 E. Ferdosi, H. Bahiraei and D. Ghanbari, *Sep. Purif. Technol.*, 2019, **211**, 35–39.

17 A. El Mragui, O. Zegaoui and J. C. G. Esteves da Silva, *Chemosphere*, 2021, **266**, 128931.

18 S. Sharma, M. Vats, J. Sharma, A. Chhabra, R. K. R. Kumar and C.-H. Chuang, *Curr. Nanosci.*, 2021, **17**, 612–619.

19 L. Yu, Q. Wang, Z. Zhang, J. He, L. Guo, K. Dong and Y. Zhang, *J. Nanosci. Nanotechnol.*, 2017, **17**, 1350–1355.

20 V. Velmurugan, U. Srinivasarao, R. Ramachandran, M. Saranya and A. N. Grace, *Mater. Res. Bull.*, 2016, **84**, 145–151.

21 Y. Zhang, Q. Shao, B. Zhao, B. Zhang, V. Murugadoss, S. Wu, T. Ding and Z. Guo, *Colloids Surf., A*, 2019, **583**, 123965.

22 M. Sharma, R. Adalati, A. Kumar, M. Mehta and R. Chandra, *ACS Appl. Mater. Interfaces*, 2022, **14**(23), 26791–26802.

23 L. Ren, B. Xu, G. Wang, X. Yin, Y. Liu, W. Yang and Y. Chen, *RSC Adv.*, 2020, **10**, 39130–39136.

24 Y. Watanabe, K. Kanazawa, Y. Komazaki, T. Nobeshima and S. Uemura, *AIP Adv.*, 2020, **10**, 035226.

25 T.-W. Kim and S.-J. Park, *J. Colloid Interface Sci.*, 2017, **486**, 287–295.

26 Y.-H. Chan, C.-Y. Tsai, Y.-J. Shih and M.-S. Wu, *Electrochim. Acta*, 2020, **364**, 137329.

27 Y. Zhang and Y. Mo, *Electrochim. Acta*, 2014, **142**, 76–83.

28 N. Parveen, M. O. Ansari, T. H. Han and M. H. Cho, *J. Solid State Electrochem.*, 2017, **21**, 57–68.

29 M. Asadzadeh, F. Tajabadi, D. Dastan, P. Sangpour, Z. Shi and N. Taghavinia, *Ceram. Int.*, 2021, **47**, 5487–5494.

30 G.-H. An, D.-Y. Lee, Y.-J. Lee and H.-J. Ahn, *ACS Appl. Mater. Interfaces*, 2016, **8**, 30264–30270.

31 M. A. Dheyab, A. A. Aziz, M. S. Jameel and N. Oladzadabbasabadi, *Surf. Interfaces*, 2022, **28**, 101677.

32 K. Selvam, C. Sudhakar, T. Selvankumar, B. Senthilkumar, W. Kim, M. M. Al-Ansari and L. Al-Humaid, *Appl. Nanosci.*, 2022, DOI: 10.1007/s13204-021-02148-0.

33 G. K. Dalapati, H. Sharma, A. Guchhait, N. Chakrabarty, P. Bamola, Q. Liu, G. Saianand, A. M. Sai Krishna, S. Mukhopadhyay, A. Dey, T. K. S. Wong, S. Zhuk, S. Ghosh, S. Chakrabortty, C. Mahata, S. Biring, A. Kumar, C. S. Ribeiro, S. Ramakrishna, A. K. Chakraborty, S. Krishnamurthy, P. Sonar and M. Sharma, *J. Mater. Chem. A*, 2021, **9**, 16621–16684.

34 K.-K. Liu, Q. Jiang, C. Kacica, H. Gholami Derami, P. Biswas and S. Singamaneni, *RSC Adv.*, 2018, **8**, 31296–31302.

35 C. Xiang, M. Li, M. Zhi, A. Manivannan and N. Wu, *J. Mater. Chem.*, 2012, **22**, 19161–19167.

36 M. Lava, U. Muddapur, N. Basavegowda, S. More and V. More, *Characterization, anticancer, antibacterial, anti-diabetic and anti-inflammatory activities of green synthesized silver nanoparticles using Justica wynaadensis leaves extract*, 2020, vol. 46.

37 H. Wang, L. Zhang, Z. Chen, J. Hu, S. Li, Z. Wang, J. Liu and X. Wang, *Chem. Soc. Rev.*, 2014, **43**, 5234–5244.

38 R. Sivaranjani, A. Thayumanavan and S. Sriram, *Bull. Mater. Sci.*, 2019, **42**, 185.

39 X. H. Vu, L. H. Phuoc, N. D. Dien, T. T. H. Pham and L. D. Thanh, *J. Electron. Mater.*, 2019, **48**, 2978–2985.

40 T. Gordon, B. Perlstein, O. Houbara, I. Felner, E. Banin and S. Margel, *Colloids Surf., A*, 2011, **374**, 1–8.

41 P. Boomi, H. G. Prabu and J. Mathiyarasu, *Colloids Surf., B*, 2013, **103**, 9–14.

42 G. R. Salunke, S. Ghosh, R. Santosh Kumar, S. Khade, P. Vashisth, T. Kale, S. Chopade, V. Pruthi, G. Kundu, J. R. Bellare and B. A. Chopade, *Int. J. Nanomed.*, 2014, **9**, 2635–2653.

43 Y. A. Arfat, J. Ahmed and H. Jacob, *Carbohydr. Polym.*, 2017, **155**, 382–390.

44 Z. Kanwal, M. A. Raza, S. Riaz, S. Manzoor, A. Tayyeb, I. Sajid and S. Naseem, *R. Soc. Open Sci.*, 2019, **6**, 182135.

45 B. S. Sivamaruthi, V. S. Ramkumar, G. Archunan, C. Chaiyasut and N. Suganthy, *J. Drug Delivery Sci. Technol.*, 2019, **51**, 139–151.

46 T. Mahvelati-Shamsabadi and E. K. Goharshadi, *Ultrason. Sonochem.*, 2017, **34**, 78–89.

47 A. Sridevi, S. Krishnamohan, M. Thairiyaraja, B. Prakash and R. Yokeshwaran, *Inorg. Chem. Commun.*, 2022, **138**, 109311.

48 N. Chandel, K. Sharma, A. Sudhaik, P. Raizada, A. Hosseini-Bandegharaei, V. K. Thakur and P. Singh, *Arabian J. Chem.*, 2020, **13**, 4324–4340.

49 X. Liu, L. Zhu, X. Wang and X. Meng, *Environ. Sci. Pollut. Res. Int.*, 2020, **27**, 13590–13598.

50 A. Bhadwal, R. Tripathi, R. Gupta, N. Kumar, R. Singh and A. Shrivastav, *RSC Adv.*, 2014, **4**, 9484–9490.

51 S. Malar, M. Venkatesan, V. Arumugam, N. Geetha, N. Saravanan, S. Murugesan, S. Ramachandran, R. Ayyasamy and A. Pugazhendhi, *Process Biochem.*, 2019, **80**, 197–202.